IEEE Access
Multidisciplinary ⋮ Rapid Review ⋮ Open Access Journal

Received 6 October 2023, accepted 11 October 2023, date of publication 23 October 2023, date of current version 10 November 2023.

Digital Object Identifier 10.1109/ACCESS.2023.3326478

RESEARCH ARTICLE

Breast Cancer Diagnosis Using Lightweight Deep Convolution Neural Network Model

TASLEEM KAUSAR[1], YUN LU[2], AND ADEEBA KAUSAR[3]

[1]Mirpur Institute of Technology, Mirpur University of Science and Technology, (MUST), Mirpur, Azad Jammu and Kashmir 10250, Pakistan
[2]School of Computer Science and Engineering, Huizhou University, Huizhou, Guangdong 516007, China
[3]Department of Information Engineering Technology, Superior University, Lahore, Punjab 05499, Pakistan

Corresponding author: Yun Lu (luyun_hit@163.com)

This work was supported in part by the Joint Fund of Basic and Applied Basic Research Fund of Guangdong Province under Grant 2020A1515110498; in part by the Fund which aims to Improve Scientific Research Capability of Key Construction Disciplines in Guangdong Province "Light-Weight Federal Learning Paradigm and its Application" under Grant 2022ZDJS058; and in part by the National Natural Science Foundation of China under Grant 62176102 and Grant 62272497.

ABSTRACT In the past few decades, breast cancer has rapidly increased the death rate among women worldwide. An early diagnosis of such fatal disease is important for the best treatment and death rate reduction. Automatic diagnosis of breast cancer from histopathological images using artificial intelligence (AI) based methods is a top-priority research area in the biomedical field. However, automatic detection is challenging due to high resolution of histopathology images and the tremendous amount of parameters required by deep AI models. Due to high computational complexity and bulky memory usage, deep models suffer from inefficient inference that limits their application in resource-constrained platforms. To address this problem, a fast cancer detection strategy has been proposed to overcome the computational cost issue of deep automatic systems. Instead of directly using input images the wavelet transform (WT) is applied to decompose the images into different frequency bands and then only low frequency bands are subjected to our proposed lightweight deep convolutional neural network (CNN). The lightweight deep model is designed using invertible residual block module. The incorporation of invertible residual block module in the deep CNN model and the use of WT considerably reduces the computational cost of the proposed model, without a noticeable accuracy downgrade Further, the effect of various machine vision classifiers i.e. support vector machine (SVM), softmax, and K nearest neighbor classifier (KNN) on model performance is analyzed. Experiments are performed using three publicly available benchmark histopathology image datasets. The proposed model has shown multi-class classification accuracy of 96.25%, and 99.8% and 72.2%, on the international conference on image analysis and recognition (ICIAR 2018), BreakHis and Bracs datasets, respectively. The reported inference time per image of the proposed model is 0.67s, and 0.21s for ICIAR 2018 and BreakHis and Bracs images, respectively.

INDEX TERMS Breast histopathology, wavelet transform, convolution neural networks, support vector machine, inverted residual block, softmax.

I. INTRODUCTION

Nowadays, breast cancer is among the most frequently recognized cancers for women according to the American Cancer Society. As per recent global cancer statistics, approximately 43,780 breast cancer deaths occurred in 2022 in the United States [1]. Timely diagnosis and prognosis of this deadly disease reduce the mortality rates and increase survivability. In the diagnostic process, the malignant growth of a tumor in breast tissues is observed through multiple examinations such as physical skin tests, mammography, and breast biopsy [2]. The biopsy examination is performed through visual inspection under the microscope which enables the pathologists to categorize the breast microscopy images into different tumor types. Through biopsy examination, two types of lesions e.g., benign and carcinomas are confirmed by pathologists. The benign lesions are non-cancerous abnormalities in the epithelial cells that usually do not cause breast cancer. The carcinomas or cancerous cells grow irregularly and are further categorized into two types of tissue classes, i.e., insitu and invasive carcinomas [3]. The manual microscopic histopathological analysis is quite challenging task due to

The associate editor coordinating the review of this manuscript and approving it for publication was Ines Domingues.

© 2023 The Authors. This work is licensed under a Creative Commons Attribution-NonCommercial-NoDerivatives 4.0 License.
For more information, see https://creativecommons.org/licenses/by-nc-nd/4.0/

its complex nature and irregular appearance of benign and carcinomas cells. Manual investigation of this kind of disease using biopsy samples always produces some contradictions by physicians. Few more limitations are also associated with manual analysis e.g., limited expertise in this field is available in hospitals, and significant effort from pathologists is required. Therefore, breast cancer type classification using the biopsy test technique could be unreliable [4].

Automatic image analysis systems can help to address the aforementioned issues [5]. The integration of digital image processing with deep learning is used in different applications of computer vision such as industrial automation, decision support systems for autonomous vehicles, the internet of things, remote sensing, and medical image analysis [6], [7], [8], [9], [10]. Currently, artificial intelligent technologies implementing machine learning (ML) as well as deep learning (DL) techniques using histopathology images are assisting radiologists to diagnose breast carcinoma, thereby improving cancer patients' status [11], [12], [13], [62], [63], [64]. These automatic methods enable the pathologists to categorize the histopathology images into different categories and also provide a second opinion to the doctors. Automatic diagnostic systems provide valuable information to physicians for disease detection [14], [15], [16]. In this regard, DL algorithms, Digital image processing, machine learning and deep learning have shown good results in various applied domains of medical image analysis [67], [68], [72].

especially convolution neural networks (CNNs) have become an optimized solution in histopathology image analysis [17], [18], [19]. In the past couple of years, several deep intelligent methods based on convolution neural networks have been developed to classify breast histopathology images into particular cancer classes [20], [21], [22].

In [23], authors suggested a CNN based model for automated classification of breast histopathology images to normal, benign, malignant, and invasive carcinoma classes and have achieved an accuracy of 87% on the ICIAR 2018 dataset. Zewdie et al. [24] designed a deep CNN and gradient boosted tree based model to perform multi-class breast cancer classification. Likewise, Araujo et al. [25] proposed a CNN and SVM based technique to extract the information at different scales. They claimed accuracy of 77.8% for four classes and 83.3% for other binary classes i.e., carcinoma or non-carcinoma classification. In [26], a concept of transfer learning was applied to deep CNN methods (GoogleNet, VGGNet, and ResNet) to improve the detection and categorization of breast cancer. In [27], Hameed et al. did the image classification of breast histopathology with the help of an ensemble of pre-trained models i.e., VGG16 and VGG19. This approach claimed an accuracy of 97.73% for the carcinoma class and 95.29% on the whole by taking the average of predicted probabilities. In [28], Yan et al. designed a hybrid convolutional and recurrent DL method and achieved an accuracy of 91.3% for the multi classification task. Recently, several CNN-based algorithms for the classification of breast cancer histopathology images have been designed for the ICIAR 2018 breast cancer histology (BACH) grand challenge dataset [29]. These proposed techniques have performed significantly by showing promising results.

Use of pre-processing techniques has shown good results in the performance of convolutional neural network models [69], [70], [71]. The preprocessing and enhancement of input histopathology images are first performed and then split into small patches, and each part is classified independently by machine vision classifiers. In [30], Vang et al. performed the patch-wise cancer type classification using the Google Inception-V3 model [31]. Then image-wise predictions are obtained with an ensemble fusion framework using majority voting and logistic regression patch-wise predictions. On the other hand, Rakhlin et al. [32] proposed a different method and they obtained sparse descriptors of smaller dimensions (1408 or 2048) from histopathology images. For the final classification results, they used gradient boosted trees. In another similar method, Awan et al. [33] extracted twelve 8192-dimensional feature vectors from a single input image utilizing the ResNet model. These feature vectors represent twelve non-overlapping patches of 512×512 pixels.

Usually, automatic cancer tumor classification is performed using histopathology images. However, automated detection of cancer tumors directly from histopathology images is complicated owing to its variability in appearance, the texture of the mitotic cells, and high-resolution of digitized pathology images [32]. Deep algorithms particularly, deep CNN models suggested in the previous literature for the detection and classification of breast cancer tumors involve high computation complexity and are difficult to train on high-resolution medical images. The computational complexity and accuracy of these models are restricted to the spatial resolution of input images. This high computational complexity of automatic deep cancer detection models makes them undesirable for real time applications. Moreover, direct processing of such high-resolution images requires a lot of GPU memory which makes it uneconomical [34]. Therefore, it is considered that automatic cancer detection is also a nontrivial solution. In the design of previously proposed deep models, the computational complexity of deep CNNs and their dependency on input image size is not taken into consideration. In a few approaches, the authors address this issue by dividing the high-resolution image into small parts (patches) and evaluating each patch independently [23]. But, it is assumed that when images are divided into small regions some mitotic cells are truncated between two nearby patches. So classification performance of the model trained on such patches is remarkably reduced. In addition, most of the publically available image datasets contain image-wise class labels despite pixel-wise annotations. So, there is no assurance of enough information for the correct tumor for the sampled small size patches with few pixels. In addition, existing CNN models always involve huge amounts of parameters and intolerant memory footprint. This high computational demand for deep models leads to inefficient inference and limits their usage in automatic detection from high resolution images.

It is interesting to see how deep CNN models can efficiently detect cancer tumors from high-resolution histopathology images.

The wavelets [35], [36] have been an effective mathematical tool to extract both the frequency and spatial information from different kinds of data and are thus widely used in computer vision applications. Along with the success of deep models, the researchers have introduced many fruitful methods to apply wavelet transform with deep CNN models [37], [38], [39] for various tasks. Williams and Li [38] designed a deep CNN model through wavelet pooling instead of using the max and average pooling. They claim that by using the discrete transform in the CNN model the global details of images remain preserved during the down sampling operation. Chen et al. [40] designed a wavelet like auto-encoder which accelerates the deep models. They accelerate the computation by compressing the size of the original image to low resolution. Fujieda et al. [41] designed a strategy that leverages the spectral details in texture classification using a wavelet transform based CNN model. Wan et al. [42] decomposed the histopathology images into wavelet subbands with dual-tree complex wavelet transform (DT-CWT). In this approach, statistical features are obtained from each subband and mitotic cell detection is performed with the SVM classifier. Similarly, Niwas et al. [43] sought a complex Daubechies wavelet transform for extraction of cell nuclei features from fine needle aspiration cytology images. Then they applied a multivariate KNN classifier to diagnose breast cancer on those extracted cell nuclei. In another technique [44], the authors performed the segmentation of cell nuclei with k-means clustering and subsequently, discrete wavelet transform (Coiflets) was used for the image segmentation. Cancer detection is performed based on entropy features extracted from the segmented sub bands by taking wavelet transforms as sampling operations.

The depth, width, and height of the input image are important for CNN expressive power to increase accuracy with the overhead of parameters. It is common practice to reduce the size (depth and width) of an over parameterized model by trading the accuracy. However, the effective design of a CNN model for real-time applications with minimum computational cost and good accuracy is quite challenging and still stands as an open question. Unlike previous approaches, this proposed strategy not only focuses on network computational cost issues but also the recognition accuracy. Our work systematically and empirically focuses on CNN model architecture (width, depth) and input image resolution. When a pathological image with high resolution is input to a deep CNN model, the goal is to accurately recognize the image into multi categories with minimum inference time. In this work, state-of-the-art techniques are explored to minimize the network parametric load without compromising its output accuracy. The novelty of this work lies in performing effective image down sampling using wavelet transform and lightweight CNN model design. Various image-down sampling techniques are applied to minimize input image size and to achieve robustness against random noises. An inverted residual block is introduced that considerably reduces the convolution time of deep CNN models and accelerates the inference computation without degrading its performance. The implementation of inverted residual blocks in deep CNN models greatly reduces the size of parameters in the designed model and provides an efficient mechanism to control computations and decrease the test time. The experimental results reveal that the computational burden of deep CNNs is reduced by using the decomposed input histopathological images with inverted residual blocks. The proposed lightweight CNN based system has proven to be effective to perform multi-class cancer type classification from large size histopathology images with essential training skills. Overall test time of the designed deep CNN model is decreased for the detection and categorization of cancer tumors. The low computational cost of the proposed approach made it optimal for envisage into real implementations. It could help pathologists to identify the cancer type with perfect consensus. In this regard, our designed method brought a new perspective to breast histopathology image analysis and it could facilitate other fields of computational pathology e.g., the categorization of colorectal polyps through whole-slide images. The main contributions are stated as:

- The image decomposition with wavelet transform is performed to achieve robustness against random noise and to reduce the computational complexity of cancer detection models.
- An intelligent lightweight deep CNN model using an IRB module is designed for multi-class cancer categorization from high-resolution microscopy histopathological images.
- Performance evaluation and comparison using different state-of-the-art deep CNN models and ML classification methods on two benchmark datasets.

The remaining parts of the paper are arranged as follows: The technical detail of methodology and datasets information is given in Section II. Experimental setup, and results discussion is provided in Section III. In the end, Section IV concludes the paper.

II. METHODOLOGY

The general workflow of the proposed scheme is given in Figure 1. At the training stage, data augmentation is performed and high-resolution pathological images are down sampled with wavelet transform to improve quantitative analysis and to reduce the computational cost of the deep CNN model. After down sampling, the low size images are input to the lightweight CNN to extract the deep features. The multi-class classification is performed later on with different machine learning classifiers. The proposed method is discussed in detail in the following sections.

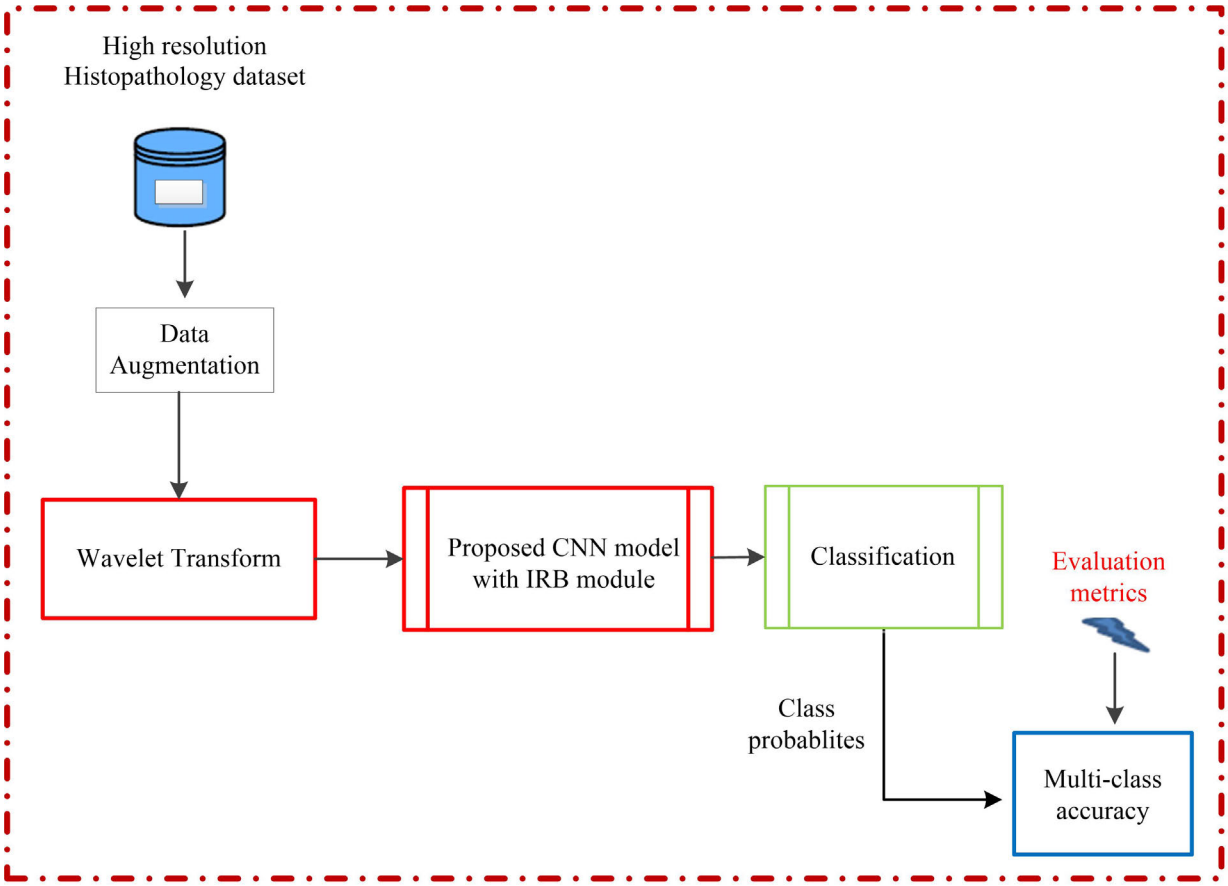

FIGURE 1. Work flow of the multi-class cancer classification with lightweight deep CNN model.

A. WAVELET TRANSFORM

The wavelets [35], [36] are mathematical tools for powerful time-frequency analysis which are broadly applied in deep learning problem solving to extract details from various data types. Our method is trying to apply wavelet transform for image decomposition of high-resolution histopathology images to reduce the commutation burden of deep CNN models. As mentioned before, the histopathology images are of high-resolution and a small portion of the image may contain the region of interest. Dividing the high-resolution image into small patches or cropping images might lose some important information about tumor type. Moreover, warping or scaling can change the shape of the region of interest due to the changes in the aspect ratio of the image. These operations can affect the classification accuracy of deep detection models. To address the issue, high-resolution images are down sampled with discrete wavelet transform before subjecting to a deep CNN model. In order to minimize computational cost and achieve higher accuracy of our proposed model, input images are down sampled with wavelet transform before subjecting them to a deep model. The discrete wavelet transform (DWT) divides the images into multiple sets of subframes into different frequency intervals and provides powerful insight into characteristics [45]. The DWT performs pyramidal image decomposition and helps to examine the local discriminative features in histopathological images [43]. In 2-D Haar wavelet decomposition, each input image (I) is convolved with a set of filters i.e. one low pass filter (W_{LL}) and three other high pass filters (W_{LH}, W_{HL}, W_{HH}) and down sampled by stride of 2. The resulting metrics are the low frequency band (LL) and three more bands of higher frequency (HL, LH, and HH). The LL band can be down sampled into LL2, LH2, HL2 HH2 bands, and so on to achieve the desired size of the image [45]. Hence, the input image of a high-resolution ($700 \times 460 \times 3$) selected from BreakHis dataset is decomposed into two level wavelets, the image will generate four matrices (LH1, HH1, HL1, LL1) of size $350 \times 230 \times 3$ and four matrices (LH2, HH2, HL2, LL2) of the size of $175 \times 115 \times 3$. The 2-level Haar wavelet decomposition makes a hierarchical structure, given in Figure 2. Three level Haar wavelet decomposed images are given in Figure 3; (a) original 700×460 pixel image taken from BreakHis dataset, (b) 1st level decomposed image, (c) 2nd level decomposed image, and (d) 3rd level decomposed image.

Using the Haar wavelet as the mother wavelet, the 2-D Haar scaling function is defined as:

$$\varphi(m, n) = \varphi(m)\varphi(n) \tag{1}$$

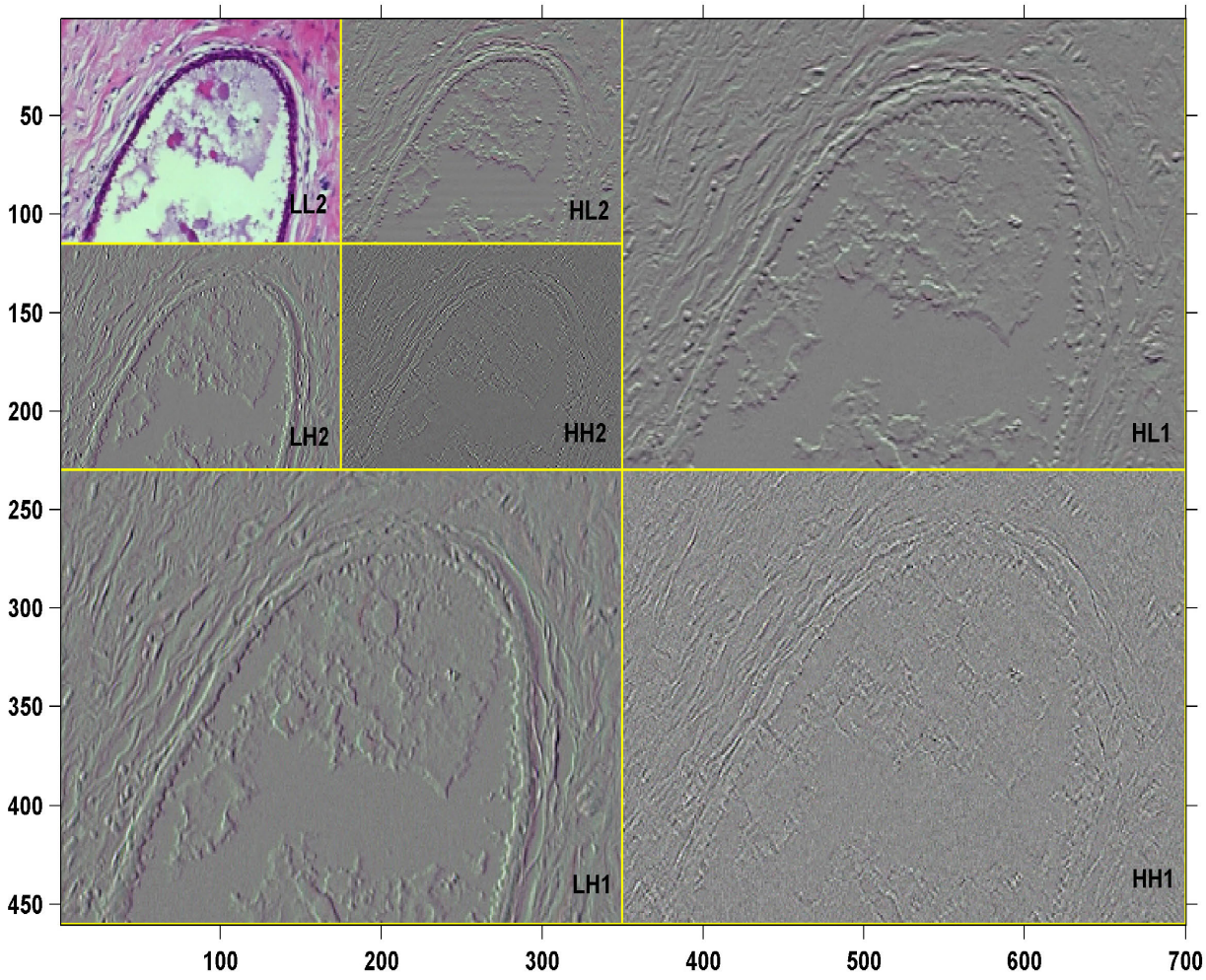

FIGURE 2. The process of pyramidal image decomposition using 2-D Haar wavelet, where LH1, HH1 & HL1 are images obtained at 1st level and LL2, HL2, LH2 & HH2 are the images obtained at 2nd level decomposition.

Corresponding three, 2-D Haar wavelets (horizontal, vertical, and diagonal) are described as:

$$\phi^H(m,n) = \phi(m)\varphi(n) \tag{2}$$

$$\phi^V(m,n) = \varphi(m)\phi(n) \tag{3}$$

$$\phi^D(x,y) = \phi(x)\phi(y) \tag{4}$$

where

$$\varphi(x) := \begin{cases} 1 & for\ 0 \le x < 1 \\ 0 & otherwise \end{cases} \tag{5}$$

$$\phi(x) := \begin{cases} 1 & for\ \ 0 \le x < 1/2 \\ -1 & for\ \ 1/2 \le x < 1 \\ 0 & elsewhere \end{cases} \tag{6}$$

Equation 5 and Equation 6 are 1-D scaling functions and corresponding wavelets, respectively

The DWT for an image I of dimensions (m, n) is given as:

$$W_\varphi(h_0,x,y) = \frac{1}{\sqrt{MN}} \sum_{m=0}^{M-1} \sum_{n=0}^{N-1} I(m,n)\varphi_{h_0}, x, y(m,n) \tag{7}$$

$$W_\phi^q(h,x,y) = \frac{1}{\sqrt{MN}} \sum_{m=0}^{M-1} \sum_{n=0}^{N-1} I(m,n)\phi_{h,x,y}^q(m,n) \tag{8}$$

where $q = \{H, V, D\}$ and $W_\varphi(h_0, x, y)$ in Equation 7 represents the approximation coefficient of the image I at scale h_0, whereas the term $W_\phi^q(h, x, y)$ in Equation 8 denotes the detail coefficients for scales $h \ge h_0$. In Equation 7, h_0 indicates the randomly selected starting scale of size 1×1, h indicates the intermediate scale of the size $2^h \times 2^h$ that varies from $0 \le h \le H$. The H represents the highest scale of size $m \times n$.

Details of the original image can be restored with inverse DWT as:

$$I(m,n) = \frac{1}{\sqrt{MN}} \sum_x \sum_y W_\varphi(h_0,x,y)\varphi_{h_0,x,y}(m,n) + \frac{1}{\sqrt{MN}} \sum_{q=H,V,D} \sum_{h=h_0}^{\infty} \sum_x \sum_y W_\phi^q(h,m,n)\phi_{h,x,y}^q(m,n) \tag{9}$$

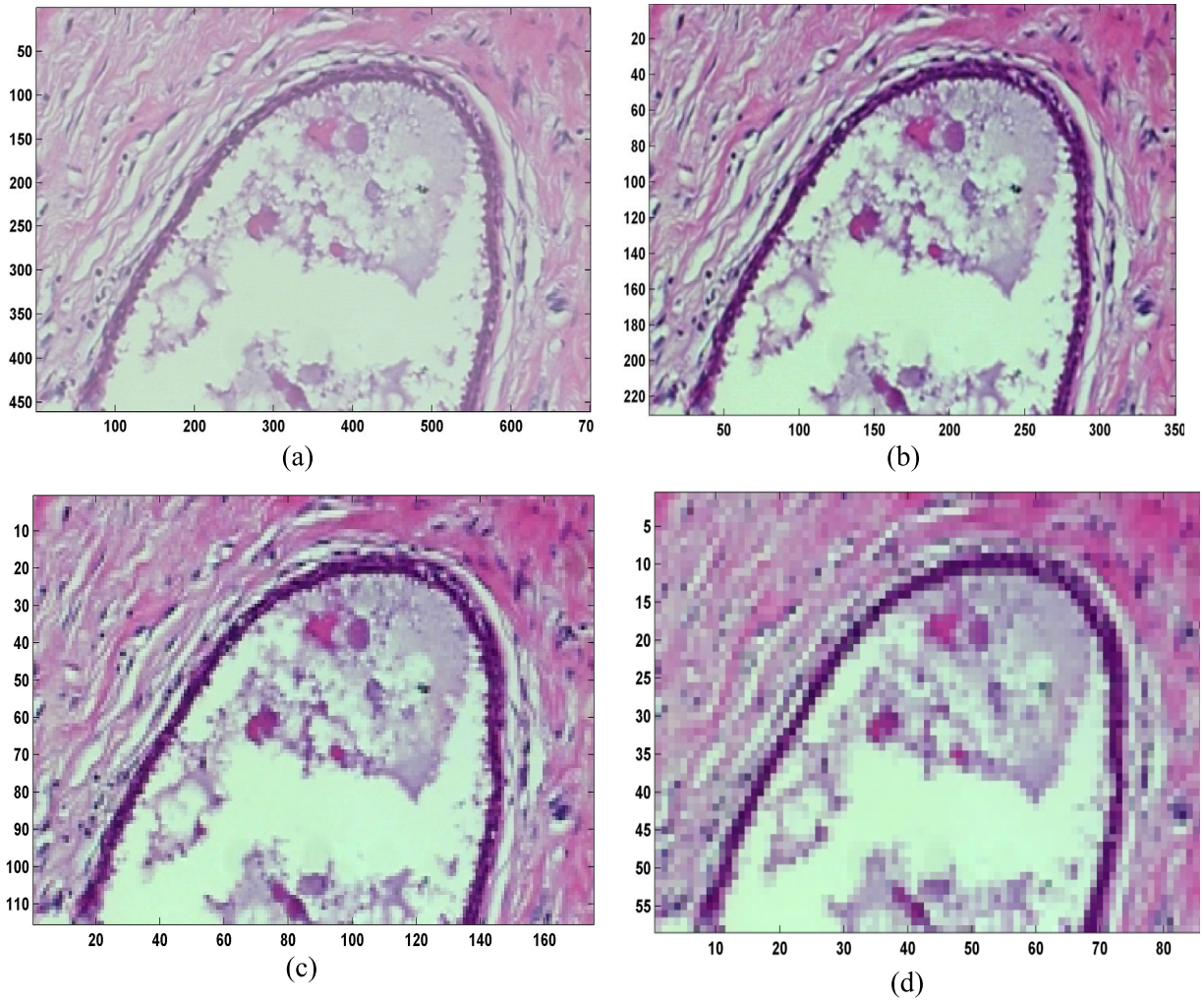

FIGURE 3. (a) Original 700 × 460 pixel image taken from BreakHis dataset, (b) 1st level decomposed image, (c) 2nd level decomposed image, (d) 3rd level decomposed image.

B. LIGHTWEIGHT DEEP CNN MODEL

In this section, various modifications are discussed that are carried out in the design of lightweight deep CNN models. For the design of our lightweight model, few state-of-the-art CNN networks like VGG16 [46], ResNet50 [47], Inceptionv3 [31], and DensNet201 [48] are selected as backbone of our model. Early networks such as VGG16 [46], ResNet50 [47], Inceptionv3 [31], and DensNet201 [48] are consists mainly of three types of alternative layers i.e. convolution, activation, max-pooling, and FC layers [49]. In these networks, the main computation cost comes from fully connected (FC) layers due to the large number of parameters involved by them. However, in literature, several strategies have been proposed to make the network more light and efficient. The transfer learning phenomenon is commonly used to transfer knowledge to a new domain from a pre-trained network. Network parametric load can be reduced by replacing the FC layers with other types of layers which offer less number of parameters. Further controlling the number of layers and optimizing the hyperparameters in conventional networks can effectively reduce the computational cost without decreasing the accuracy. The architecture of the proposed model with DenseNet201 backbone is presented in Figure 4.

In this designed method, the computation cost issue is controlled by using depthwise separable convolution (DSC) convolution layer which involves fewer parameters. The DSC is a drop-in replacement of standard convolution in which convolution operation is performed with depthwise convolution (lightweight filtering) and 1 × 1 pointwise convolution. Depthwise convolution extracted the feature maps using a single convolutional filter and subsequently, 1 × 1 pointwise convolution is used to combine the extracted features. However, in traditional convolution (TC) feature extraction and fusion are performed at the same time, from parameter perspectives with TC the obtained efficiency is low, and the computational cost is high. The DSC initially introduced the concept of 1 × 1 pointwise convolution, later MobileNetV2 [50] proposed the inverted residual

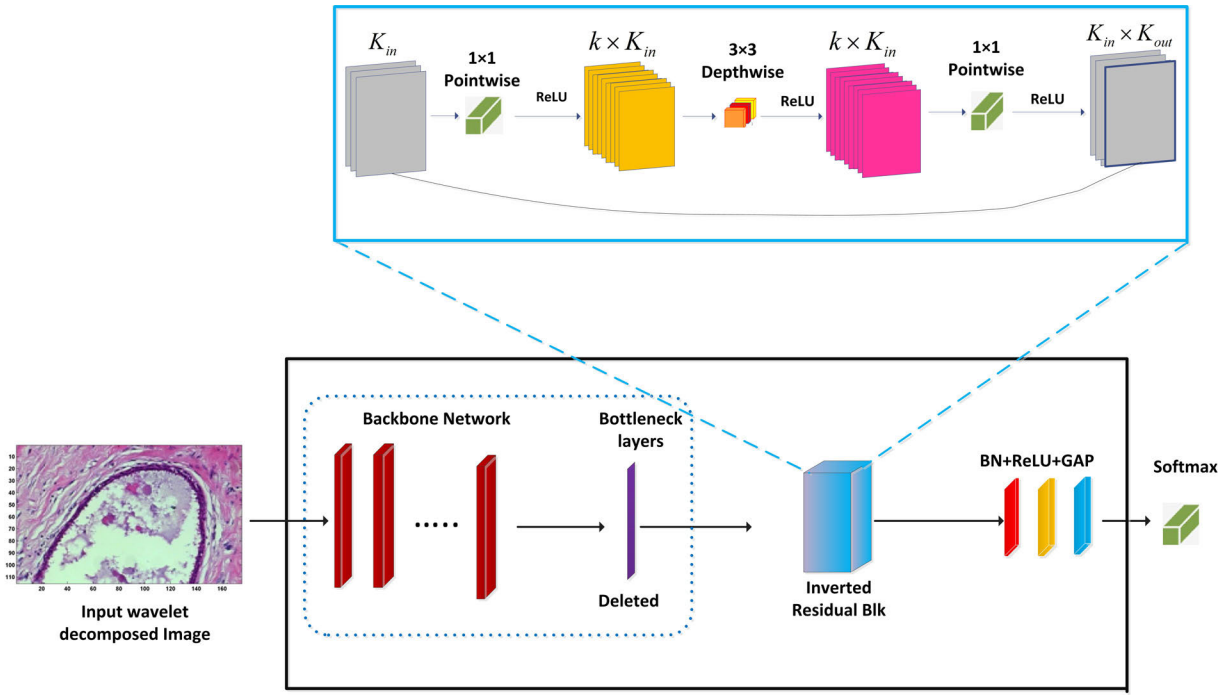

FIGURE 4. Proposed framework (with DenseNet201 backbone) for multi-classes cancer classification of histopathology images.

block which improves the DSC operation and makes the network fast with better performance. In our, each selected backbone network (VGG16 [46], ResNet50 [47], Inceptionv3 [31], and DensNet201) last few modules are replaced with invertible residual block modules involving lesser number of parameters. For the baseline ResNet50 model, the last six convolution layers are replaced with an invertible residual block module. For the baseline InceptionV3 model, the inception module at the end is replaced with an invertible residual block module. The original DenseNet201 model consists of four dense blocks and a transition layers. The adjacent dense blocks are joined by transition layer (having 1×1 convolution followed by 2×2 average pooling). Every dense block contains bottleneck layers of 6, 12, 48, 32, respectively. BN-ReLU-1 $\times$ 1Conv-BN-ReLU-3 $\times$ 3 Conv is used in each bottleneck layer, where Conv represents convolution and BN denotes the batch normalization operation. For the baseline DenseNet201 model, 10 Bottleneck layers in the last dense block are replaced with an invertible residual block module. The architecture of the proposed model (with DenseNet201 backbone) is given in Table1.

In the invertible residual block module, convolution is performed using 1×1 pointwise convolution and depth wise convolution. Because such convolution (depth wise) cannot change the output channels, the amount of channels of output featured map (K_{out}) remains the same as of channels of the input featured map (K_{in}). Therefore, a pointwise convolution of the size of 1×1 is added before and afterward depth wise convolution in the invertible residual block module. The first pointwise convolutional layer expanded the output featured maps by a factor k. The channels in feature maps output are increased $k \times K_{in}$. The second point wise convolution layer reduces the output channels as the input channels and concentrates the feature information. In the meantime, the module also includes a shortcut connection. The proposed model extracts features in bigger dimensional space thus improving the model performance. In the invertible residual block module, the value of the expansion ratio k is set as 2. Finally, the convolution layer (Conv), batch normalization layer (BN), ReLU activation function (ReLU), global average pooling (GAP), and Softmax are added to the network. Figure 4 shows an overview of the proposed deep CNN model. The incorporation of suggested modifications in the proposed model reduces the network parametric load and ultimately decreases the computational cost.

C. COMPUTATIONAL COMPLEXITY AND TEST TIME OPTIMIZATION

In CNN architecture, the time computations involved by any standard convolution layer are computed in terms of size of input feature map K_{in} from the previous layer, kernel size $f \times f$, and the number of channels of output feature maps K_{out} as [61]:

$$O_{std}\left(m_{in} \cdot n_{in} \cdot K_{in} \cdot f^2 \cdot K_{out}\right) \tag{10}$$

where, m_{in}, n_{in} and K_{out} are spatial dimensions of the input image. Equation 10 shows that the time complexity of CNN architecture mostly depends on input image size, kernel size, and the number of kernels used in the output layer. In our

TABLE 1. The architecture of the proposed model (with densenet201 backbone using expansion factor=2).

Layer	The proposed model (with DenseNet201 backbone)	Input shape	Output shape
Input		512×384×3	512×384×3
Convolution	7 × 7 conv, stride 2	512×384×3	256×192×96
Pool	3 × 3 max pool, stride 2	256×192×96	128×96×96
Dense block (1)	$\begin{bmatrix} 1\times1\ conv \\ 3\times3\ conv \end{bmatrix}\times6$	128×96×96	128×96×384
Transition layer	1 × 1 conv 2 × 2 average pool, stride 2	128×96×384 128×96×192	128×96×192 64×48×192
Dense block (2)	$\begin{bmatrix} 1\times1\ conv \\ 3\times3\ conv \end{bmatrix}\times12$	64×48×192	64×48×768
Transition layer	1 × 1 conv 2 × 2 average pool, stride 2	64×48×768 32×24×1056	64×48×384 16×12×1056
Dense block (3)	$\begin{bmatrix} 1\times1\ conv \\ 3\times3\ conv \end{bmatrix}\times48$	32×24×384	32×24×3072
Transition layer	1 × 1 conv 2 × 2 average pool, stride 2	32×24×3072 32×24×1056	32×24×1056 16×12×1056
Dense block (4)	$\begin{bmatrix} 1\times1\ conv \\ 3\times3\ conv \end{bmatrix}\times22$	16×12×1056	16×12×1408
IRB block	1x1 conv 3x3 dwise, stride=2, expansion factor=2 1x1 conv	16×12×1408 16×12×2816 8×6×2816	16×12×2816 8×6×2816 8×6×1408
Classification	GAP Softmax	8×6×1408 1×1×1408	1×1×1408 4

designed architecture, the invertible residual block module and down sampling effect of wavelet transform majorly contribute to computational complexity reduction.

1) COMPUTATIONS MINIMIZATION WITH INVERTIBLE RESIDUAL BLOCK MODULE

The implementation of the invertible residual block [50] module in the CNN model effectively minimizes the computational burden of deep models. The invertible residual block module uses the DSC layer that divides the standard convolution into i) depthwise convolution and ii) 1 × 1 pointwise convolution. Overall, the computational price of DSC is calculated in terms of deep convolution and 1 × 1 convolution as:

$$O_{dcs}\left(m_{in}\cdot n_{in}\cdot K_{in}\cdot f^2+m_{in}\cdot n_{in}\cdot K_{in}\cdot K_{out}\right) \tag{11}$$

The cost ratio of DSC to standard convolution can be calculated by dividing Equation 11 by Equation 10 as:

$$c_r=\frac{O_{dcs}\left(m_{in}\cdot n_{in}\cdot K_{in}\cdot f^2+m_{in}\cdot n_{in}\cdot K_{in}\cdot K_{out}\right)}{O_{std}\left(m_{in}\cdot n_{in}\cdot K_{in}\cdot f^2\cdot K_{out}\right)} \tag{12}$$

$$c_r=1/K_{out}+1/f^2 \tag{13}$$

The computation cost ratio evaluated in Equation 13 represents that multiplication operation is split into multiplication and addition operations due to that the computational cost is significantly reduced.

For instance, if the original input image from ICIAR 2018 dataset is subjected to deep CNN model with invertible residual block model, at the first layer, in depth wise convolution layer, 3 3 × 3 × 1 filters move 2048 × 1536 times (i.e., 3 × 3 × 3 × 2048 × 1536 = 84,934,656 multiplications). Similarly, in the case of point-to-point convolution, 64 1 × 1 × 3 filters move 2048 × 1536 times (i.e., 64 × 1 × 1 × 3 × 2048 × 1536=603,979,776 multiplications). The cumulative sum of multiplications involves depthwise convolution and a point wise convolution is 688,914,432 multiplications.

However, in the case of standard convolution, 64 3 × 3 × 3 filters move 2048 × 1536 times (i.e., 64 × 3 × 3 × 3 × 2048 × 1536=5,435,817,984 multiplications). The value of c_r computed using Equation 13 is 12.6% which shows that time costs at the first convolution layer are reduced by 87.32%. The comparison of the calculations performed with an invertible residual block module and standard convolution shows that down sampled invertible residual block majorly contributes to decreasing the computational cost.

2) COMPUTATIONS MINIMIZATION BOTH WITH INVERTIBLE RESIDUAL BLOCK MODULE AND WAVELET TRANSFORM

When the resolution of the input image is down sampled from 2048 × 1536×3 to 512 × 384×3 using 2-D Haar wavelet transform and inputted to our designed deep CNN model having invertible residual block module the overall time complexity is further reduced to 95% and is computed (using Equation 11) as:

$$O_{dcs}$$
$$(2048\times1536\times3\times3^2+1\times1\times2048\times1536\times3\times64)$$

to $O_{dcs}(512 \times 384 \times 3 \times 3^2 + 1 \times 1 \times 512 \times 384 \times 3 \times 64)$ i.e.$\sim$ 93.72%

D. DATASETS

1) ICIAR 2018 DATASET [61]

This data is available with ICIAR 2018 breast cancer histology (BACH) grand challenge.[1] This dataset contains 400 images including 300 train and 100 test microscopy images of 2048 $\times$ 1536$\times$3 pixel resolution. Images of this dataset are obtained with a LeicaDM 335 LED microscope having 0.42 $\times$ 0.42 μm/pixel resolution. The two expert pathologists labeled these images into four cancer categories: normal, benign, insitu, and invasive carcinoma. The class labels of training data are publically available, while class labels of test data are not publically available. The image resolution of microscopy images belonging to this dataset is very high so we consider that the ICIAR 2018 dataset is more appropriate to validate the computation cost of the proposed model. In our experiments, the input images of 2048 $\times$ 1536$\times$3 pixels are down-sampled to 512 $\times$ 384$\times$3 using 2-level Haar wavelet transform. These decomposed images are then input to the deep CNN network.

2) BREAKHIS DATASET [3]

To further assess the model performance for the multi-class classification, we used another benchmark histopathological image dataset i.e. BreakHis[2] dataset. This dataset includes 7909 images of 700 $\times$ 460$\times$3 pixels belonging to two main classes: benign and malignant. Further benign class is divided into four subclasses adenosis (A), phyllodes tumor (PT), fibroadenoma (F), and tubular adenoma (TA) classes. Similarly, malignant tumors are categorized into four subclasses: ductal carcinoma (DC), mucinous carcinoma (MC), lobular carcinoma (LC), and papillary carcinoma (PC) classes. The images are scanned with a microscope of intensified factors, i.e., image $\times$40, $\times$100, $\times$200, and $\times$400. The detailed distribution of this dataset is given in Table 3. The images (700 $\times$ 460$\times$3 pixels) of the BreakHis dataset are down-sampled to 175 $\times$ 115$\times$3pixels with 2-level Haar wavelet transform before input to deep CNN model.

3) BREAST CARCINOMA SUBTYPING (BRACS) DATASET [65]

Experiments are also performed on a recent benchmark Bracs[3] dataset of whole slide hematoxylin and eosin-stained histopathological images for automated detection/classification of breast tumors. This dataset is available with The Bracs dataset is composed of 547 WSIs belonging to 189 different patients. The slides are scanned with an Aperio AT2 scanner at 0.25 μm/pixel having magnification factor of 40$\times$. The detailed distribution of this dataset according to the lesion type is given in Table 2. The Table 2 reports the number of WSIs (with and without RoIs) and RoIs and subtypes, respectively. Among the 547 WSIs, 265 belong to benign, 89 belong to Atypical, and 193 belong to malignant tumor class. To perform the experiments, Among the 547 slides, 395 were considered in train set, 67 in validation set and 85 considered in test set.

TABLE 2. The detailed distribution of bracs dataset according to the lesion type.

Data	Benign	Atypical	Malignant	Total
WSIs with ROIs	149	75	163	387
WSIs without ROIs	116	14	30	160
WSIs	265	89	193	547
ROIs	1834	1263	1439	4539

III. EXPERIMENTAL SETTINGS AND RESULTS ANALYSIS

In this part, the setting of the experiments and output results are discussed. The experiments are performed both on ICIAR 2018 and BreakHis datasets. The ICIAR 2018 dataset has 300 training images and 100 test images. In the case of the ICIAR 2018 dataset, training images are split into train and validation parts. 70% of the data is considered for training and 30% is used for validation. To avoid network overfitting and increase model performance, the size of training data is increased by generating the augmented diversities of original images. The training dataset is augmented using rotation, scaling, and elastic deformation; these augmentations achieved morphology invariance and increased the size of training data by 7 times i.e., 3 rotations + 2 scalings + 2 elastic deformations. In the case of the BreakHis dataset, the experiments are conducted on the images obtained at $\times$40 magnification factors. From the BreakHis dataset, about 30% of data (598 images) is selected in the testing set, while the remaining 70% (1397 images) is selected in the training set as per the work in [12], [33], and [34]. Like the ICIAR 2018 dataset, the size of BreakHis training data is increased to seven times using rotation, elastic deformation, and scaling techniques. The input images are decomposed using the Haar wavelet transform and then utilized in the training of the proposed model.

Image augmentations and wavelet decomposition is performed using MATLAB R2014a program while the proposed deep CNN model is implemented on TensorFlow [35] library on 2.4 GHz Intel(R) Xeon(R) E5-2630 CPU with one NVIDIA Tesla M40 GPU with a memory of 12GB. Training is started with a pre-trained backbone model (ImageNet-1K dataset [49]) where the weights of final layers are updated using the histopathology dataset to drive predictions. The weights of earlier layers are kept intact thus, the model gained the benefit of transferred features (curves and edges details) learned from the ImageNet dataset. In multi-class recognition

[1] https://iciar2018-challenge.grand-challenge.org

[2] https://web.inf.ufpr.br/vri/databases/breast-cancer-histopathological-database-breakhis/

[3] https://www.bracs.icar.cnr.it/

TABLE 3. Image distribution of breakhis dataset for main and sub-categories.

Class	Subcategories	Magnifications				Total
		40 X	100X	200X	400X	
Benign	A	114	113	111	106	444
	F	253	260	264	237	1014
	TA	109	121	108	115	453
	PT	149	150	140	130	569
Malignant	DC	864	903	896	788	3451
	LC	156	170	163	137	626
	MC	205	222	196	169	792
	PC	145	142	135	138	560
Total		1995	2081	2013	1820	7909

TABLE 4. Hyper-parameter settings used for ICIAR 2018 and breakhis (40X) datasets.

Experiments	Learning rate	Batch size	Epochs	Training Time
1	0.0001	256	90	2250s
2	0.0003	64	130	3990s
3	**0.0002**	**8**	**150**	**4200s**

models, the classification is mainly performed with a softmax classifier. In the learning phase, trainable parameters are updated by minimizing the categorical cross entropy loss function which indicates the proximity between predicted and desired output. The categorical cross entropy loss function is computed as:

$$J = \frac{1}{N}\sum_{n=1}^{N} -\log\left(\frac{e^{y_l}}{\sum_{t=1}^{T} e^{yt}}\right) \tag{14}$$

where N, y_i and j denote the training images, input to the softmax, and the number of categories, respectively. where $t = 1, 2, 3 \ldots\ldots T$, T represents total number of classes.

The quantitative performance of the model is computed based on the following metrics.

$$Sensitivity = \frac{TP}{TP + FN} \tag{15}$$

$$\Pr ecision = \frac{TP}{TP + FP} \tag{16}$$

$$Specificty = \frac{TN}{TN + FP} \tag{17}$$

$$F\ score = 2 \times \frac{precision \times sensitivity}{precision + sensitivity} \tag{18}$$

where,TP, FP&FN are the total number of true positives, false positives, and false negatives, respectively.

The experiments are performed by setting different values of hyper-parameters. These hyper-parameter settings help in training the model properly. The experiments are revised by adjusting hyper-parameters values to obtain the best performance. After different rounds of experiments using the training dataset, the optimal values of hyper-parameters are chosen. The hyper parameters values and training time is given in Table 4. In the first experiment, the model is trained for 90 epochs using a learning rate of 0.0001. Similarly, in the second experiment model is trained for 130 epochs using learning rate of 0.0003, and the best performance is obtained when the model is trained for 150 epochs using learning rate of 0.0002 and batch size of 8 with root mean square propagation (rmsprop) optimizer. The same experimental settings are followed for model training on BreakHis data.

In order to check the effect of data augmentation on model performance, few experiments are performed with images that are augmented with rotation, scaling, and elastic deformation techniques. Results obtained by incorporating different data augmentation techniques are reported in Table 5. Firstly, the model is trained on the original set of images. Secondly, the model is trained on the augmented images that are rotated using preset values of 45°, 90°, 135°, 220°, and 180°. In the third experiment, the model is trained on images deformed with the elastic deformation method proposed in [51]. The training images are deformed by setting the elasticity coefficient (σ) to 10 and the scaling factor (α) to 90. In the fourth experiment, images are scaled with the nearest-neighbor interpolation method. Reference [52] considering a zooming factor of 0.85 and 0.95. In the fifth experiment, performance is obtained by involving rotation, deformation, scaling, and wavelet decomposition.

To examine the effectiveness of Haar wavelet image decomposition on model performance, experiments are performed using different levels of Haar wavelet decomposed images selected from the ICIAR 2018 dataset. The experimental outcomes are reported in Table 6. Firstly, the model is trained based on original images of high resolution. In the second, third, and fourth experiments, the model is trained on 1st, 2nd, and 3rd level decomposed images, respectively. The results provided in Table 6 show that the best performance in terms of computational cost and accuracy is obtained when the proposed model is trained with 2nd level decomposed images of size of 512 × 384×3 pixels. It is because of the high signal-to-noise power of the decomposed image (512 × 384×3) of 2nd level compared to 1st level decomposed image (1024 × 768×3). Similarly, the classification efficiency reduces to 95% when the model is

TABLE 5. Analysis with different data augmentations (ROTATIONS, SCALING, ELASTIC DEFORMATION) using ICIAR 2018 dataset.

Experiments	Techniques	Precision (%)	Sensitivity (%)	Specificity (%)	F score (%)	Accuracy (%)
1	Proposed method trained on the original set	95.3	94.9	93.8	95.2.	93.2
2	Proposed method+ augmented data involving rotation	96.7	96.4	97.2	96.5	93.5
3	Proposed method+ augmented data involving deformation	97.0	97.2	97.1	97.1	94.6
4	Proposed method+ augmented data involving scaling	99.1	99.2	98.7	99.1	95.1
5	**Proposed method+** rotation+ deformation+ scaling+ wavelet decomposition	**99.8**	**99.4**	**99.0**	**99.5**	**96.2**

TABLE 6. Average accuracy and test time performance on ICIAR 2018 and breakhis dataset using 1st, 2nd, and 3rd level decomposed images.

	ICIAR dataset				BreakHis dataset (40X)		
Experiments	Image	Resolution of image	Test time per image (s)	Accuracy (%)	Resolution of image	Test time per image (s)	Accuracy (%)
1	Original size	2048×1536×3	4.01	98.1	700×460×3	1.1	99.9
2	1st level decomposed	1024 ×768 ×3	1.3	97.2	350 ×230 ×3	0.54	99.2
3	**2nd level decomposed**	**512 ×384×3**	**0.67**	**96.25**	**175 ×115×3**	**0.21**	**99.8**
4	3rd level decomposed	256×192×3	0.43	95.0	88×58×3	0.12	98.3

trained on 3rd level decomposed image of size 256 × 192×3. It is due to the recurring combination of max-pooling and striding in deep CNN which lost a lot of information from the output feature. On the contrary, the model trained with original size images represents little high accuracy (1.88%) compared with the model trained on 2nd level decomposed images, it's because of the image decomposition step, which lost little information from input images. However, the test time per image of the model trained with the original size image is very high (83.2%), compared to the model trained on decomposed images. Thus, 2nd level decomposed images are used in our experiments, to perform multi-level cancer type classification. The 2-level wavelet decomposition of high-resolution histopathology images vastly reduced the computational burden of our designed CNN model and made possible fast cancer classification with GPU computing.

To check the effectiveness of the Haar wavelet transform over other decomposition techniques, the experiments are also performed using the other wavelets. Images are downs ampled with two types of wavelets: Daubechies and Coiflets. The proposed model is trained separately on each type of down sampled image. Binary class and multi-class classification results obtained using Haar, Daubechies, and Coiflets decomposed images are reported in Table 7. In comparison to other decomposition techniques, the model trained on 2-level Haar wavelet decomposed images shows the best performance.

Besides, the recognition performance and recognition speed of cancer detection systems are important. In a real-time scenario, it is the foremost priority to make the detection speed fast. Our model took 0.68s and 0.21s on ICIAR 2018 and BreakHis datasets for a single image. Low test time in the case of our method is due to the use of an invertible residual block module, the appropriate setting of expansion ratio k in the invertible residual block module, and down sampled image which reduces the memory requirement and inference time.

Since the classification performance is influenced by the architecture of the backbone network. Therefore, experiments are performed with different backbone networks by setting the different values of expansion ratio k in the invertible residual block module of our proposed model. The accuracy and test time per image both on ICIAR 2018 and BreakHis dataset (40X magnification images) are given in Table 8 and Table 9. As evident from the results (reported in Table 8 and Table 9), our model with different baselines obtains improvement to different degrees. Meanwhile, it is important to note that there is little impact of change in factor k on accuracy. However, test time increases as the value k increases from $k = 1$ to $k = 2$ to $k = 3$. It is

TABLE 7. The multi-class and binary-class classification using ICIAR 2018 images decomposed with different wavelets for the validation data.

		Multi-class				Binary-class				
Wavelets	Datasets	Precision (%)	Sensitivity (%)	Specificity (%)	F score (%)	Precision (%)	Sensitivity (%)	Specificity (%)	F score (%)	Test time per image (s)
Original size image	ICIAR 2018	99.3	99.0	98.2	99.2	99.4	99.6	99.1	99.5	4.0
	BreakHis	99.2	99.6	99.1	99.4	99.9	100	99.3	99.8	1.1
Daubechies (db2) decomposed	ICIAR 2018	92.9	93.3	93.1	93.1	95.1	95.4	93.7	95.3	0.69
	BreakHis	95. 4	95.1	94.2	95.3	93.3	93.9	94.4	93.6	0.24
Coiflets (coif 2) decomposed	ICIAR 2018	93.1	92.5	91.7	92.8	95.0	94.1	91.9	94.3	0.72
	BreakHis	94.0	95.0	94.8	94.9	94.8	95.6	95.2	95.3	0.23
Haar wavelet decomposed)	**ICIAR 2018**	**97.8**	**96.8**	**95.0**	**97.1**	**98.4**	**98.6**	**97.3**	**98.5**	**0.68**
	BreakHis	**99.5**	**99.8**	**99.2**	**99.6**	**99.9**	**100**	**99.5**	**99.9**	**0.21**

TABLE 8. Accuracy and test time per image comparison of our modified network using different backbones and with change of factor k value on ICIAR 2018 dataset.

	k =1			k **=2**			k =3		
Proposed method with Backbone:	Accuracy (%)	Parameters	Test time (s)	Accuracy (%)	Parameters	Test time (s)	Accuracy (%)	Parameters	Test time (s)
DenseNet201 [48]	93.4	18,430,747	0.52	**96.2**	**26,706,764**	**0.67**	96.9	32,080,252	0.8
InceptionV3 [53]	89.7	21,611,487	1.1	92.1	28,830,234	1.4	93.1	33,902,231	1.3
ResNet50 [47]	88.2	141,231,342	1.3	89.1	149,361,165	1.6	91.6	156,410,123	1.9
VGG16 [46]	82.3	29,430,123	1.0	84.4	34,50,231	1.3	86.2	39,630,456	1.2

TABLE 9. Accuracy and test time per image comparison of our modified model using different baslines and with change of factor k value on breakhis dataset (40X).

	k =1			k **=2**			k =3		
Proposed method with Backbone:	Accuracy (%)	Parameters	Test time (s)	Accuracy (%)	Parameters	Test time (s)	Accuracy (%)	Parameters	Test time (s)
DenseNet201 [48]	97.4	18,430,747	0.19	**99.4**	**26,706,764**	**0.21**	**99.8**	32,080,252	0.34
InceptionV3 [53]	94.3	21,611,487	1.2	95.4	28,830,234	1.4	96.3	33,902,231	1.6
ResNet50 [47]	92.6	141,231,342	1.7	93.8	149,361,165	2.1	91.6	156,410,123	2.9
VGG16 [46]	86.3	29,430,123	1.0	88.1	34,50,231	1.2	89.0	39,630,456	1.4

because the parameters rise sharply by increasing the k value. In our experiments, the Inception.v3 network is used as the backbone network and set the $k = 2$. This setting helps in obtaining significant accuracy with optimal test time.

Moreover, we performed the performance comparison of the designed model (Backbone: DenseNet201 using IRB with =2) with state-of-the-art models (without using the IRB module). The comparative analysis given in Table 10 demonstrates that our modified model has fewer parameters and has shown better accuracy compared to the corresponding original state-of-the-art DenseNet201, InceptionV3, ResNet50, and VGG16 networks. The performance of the proposed model is also evaluated using three state-of-the-art machine vision classifiers: support vector machine (SVM), K nearest neighbor classifier (KNN), and softmax classifier. From the results (reported in Table 11), it is found that the

TABLE 10. Accuracy and test time comparison of proposed model with original state-of-the-art models using ICIAR 2018 dataset.

Method	Accuracy (%)	Parameters	Test time (s)
Proposed model (Backbone: DenseNet201 using IRB with k =2)	96.2	26,706,764	0.67
Original DenseNet201 (without IRB module)	95.1	27,110,731	1.4
Original InceptionV3 (without IRB module)	93.1	29,122,244	2.0
Original ResNet50 (without IRB module)	88.1	153,345,230	2.3
Original VGG16 (without IRB module)	82.8	41,23,261	1.8

TABLE 11. Multi-class classification performance using different machine vision classifiers on 2nd level haar wavelet decomposed ICIAR 2018 AND breakhis (40X) datasets.

Dataset		Proposed model-SVM	Proposed model-KNN	**Proposed model-Softmax**
ICIAR 2018	Precision (%)	90.7	92.9	**97.0**
	Sensitivity (%)	92.6	93.2	**99.2**
	F score (%)	91.8	93.1	**97.1**
BreakHis	Precision (%)	96.8	93.4	**99.1**
	Sensitivity (%)	95.9	93.8	**98.8**
	F score (%)	96.3	93.9	**98.6**

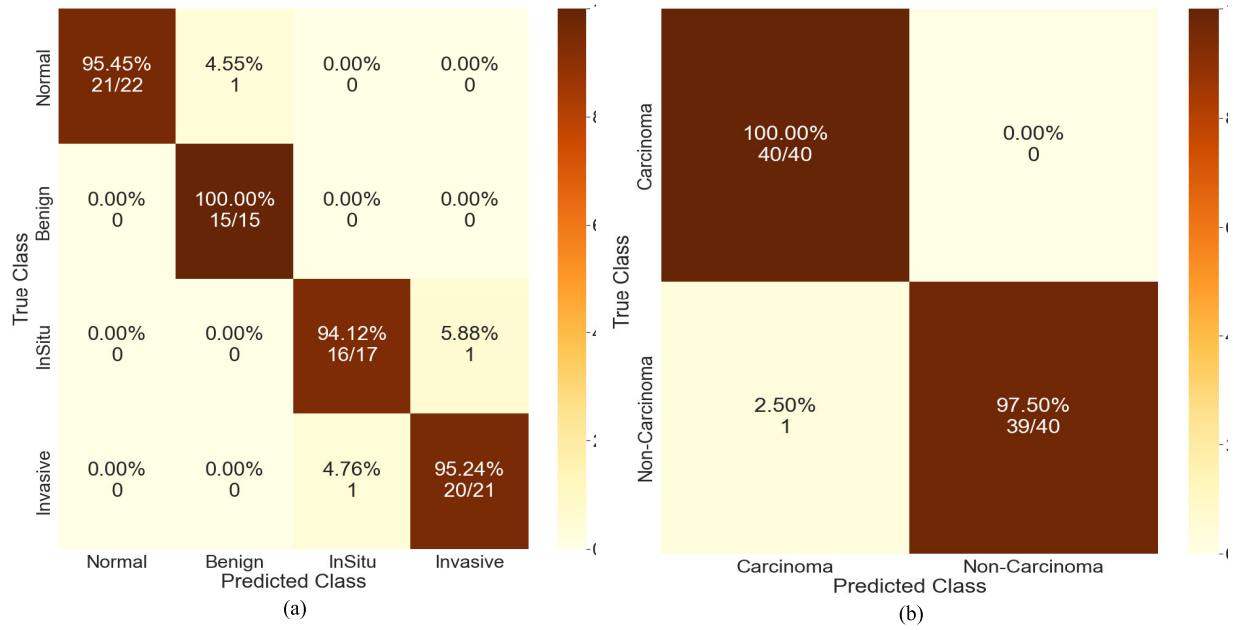

FIGURE 5. The confusion matrix of the proposed model (a) multi-class and (b) binary class classification using the validation part of the ICIAR 2018 dataset.

softmax algorithm is the most accurate among the three tested algorithms.

The confusion matrix of the proposed model for binary class (Figure 5a) and multi-class (Figure 5b) classification using the validation part of the ICIAR 2018 dataset is given in Figure 5. In comparison to binary class performance, the model reflects relatively low accuracy for multi-class classification. It is due to the numerous morphological features that are similar in intra-class images: normal & benign class and in insitu & invasive class. Few images are misclassified from the category insitu class to invasive class. Examples of a few misclassified images from the validation set are given in Figure 6. In Figure 6(a), most of the lumen structure is repeated in normal and benign classes. During

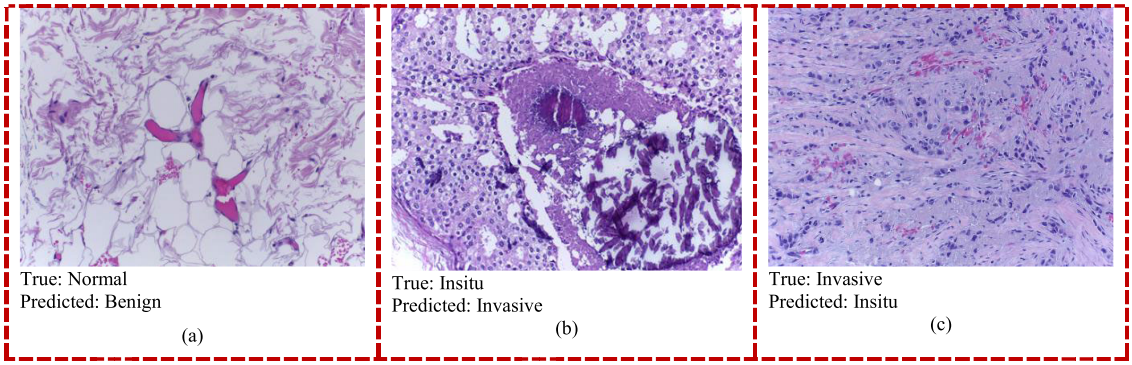

FIGURE 6. Examples of misclassified images from the validation part of the ICIAR 2018 dataset.

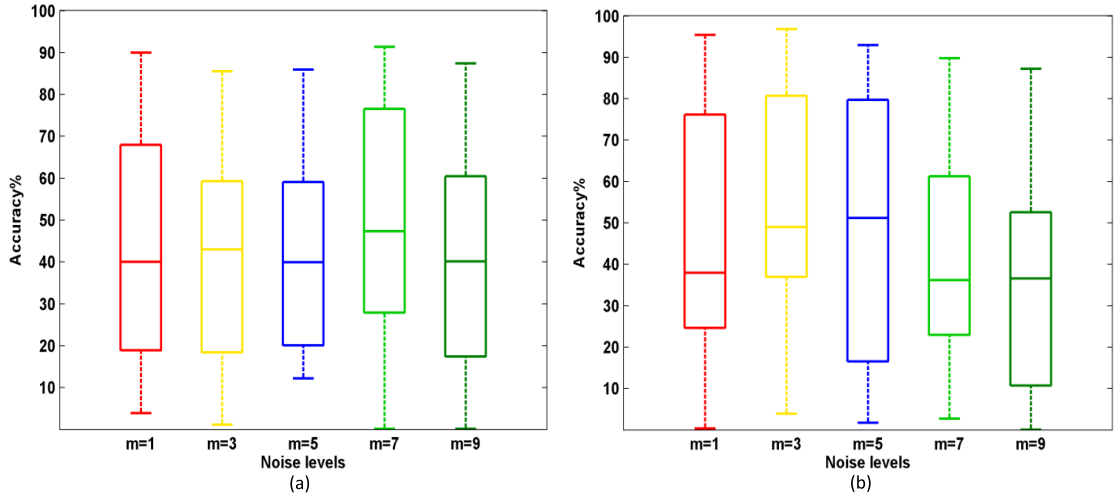

FIGURE 7. Accuracy graph using (a) ICIAR 2018 and (b) BreakHis (40X) contaminated with different levels of noise.

TABLE 12. Accuracy comparison with state-of-the-art methods reported in [29] on 2^{ND} level decomposed ICIAR 2018 hidden test dataset.

Method	Accuracy (%)
Our proposed model	92
Chennamsetty et al.	87
Kwok	87
Brancati et al.	86
Marami et al.	84
Kohl et al.	83
Wang et al.	83
Steinfeldt et al.	81
Kone et al.	81
Nedjar et al.	81
Ravi et al.	80
Wang et al.	79
Cao et al.	79
Seo et al.	79
Sidhom et al.	78
Guo et al.	77
Ranjan et al.	77
Mahbod et al.	77

the testing phase, our model misclassified the normal class image as benign class. Where in Figure 6(b), nuclei of some of the luminal structures tend to enlarge, leading the proposed model to classify the image insitu class as invasive class. Figure 6(c) shows an image from the invasive category with blebs, the model misclassified it as insitu class owing to the presence of blebs.

A. DETECTION ROBUSTNESS OF THE PROPOSED MODEL AGAINST RANDOM MULTIPLICATIVE AND ADDITIVE NOISES

The histopathological images acquired from different laboratories using different devices are often contaminated with noises. These noise perturbations mislead deep CNNs to the wrong detection. To test the robustness of the model against the noises, different levels of Gaussian noises $\overline{I} = I + m.randn(c_1, c_2.3)$ are added to Haar wavelet decomposed test images. Where $\overline{I}$ denotes the contaminated image of the original image I of size$c_1 \times c_2 \times 3$. The $randn()$ indicates the Gaussian noise function. Experiments are performed by using the noise levels values $n = 0.5$, and $m = 1, 3, 5, 7, 9$. The contaminated data was given as input to the model and the output is monitored. On both datasets: ICIAR 2018 and BreakHis, minor decreases in accuracy occurred for different levels of noise. The accuracies obtained on test images

TABLE 13. Accuracy (in %) comparison with state-of-the-art methods using 2^{ND} level decomposed breakhis (40X, 100X, 200X, and 400X magnification factors) test dataset.

Method	40X	100X	200X	400X
Spanhol et al. [54]	93.50 %	89.00 %	87.00 %	82.50 %
Nahid et al. [57]	94.40 %	95.93 %	97.19 %	96.00 %
M.Z. Alom et al. [55]	98.50 %	98.00 %	98.00 %	97.50 %
Zhongyi Han et al.[56]	98.50 %	97.50 %	97.00 %	96.00 %
Gupta et al.[58]	99.54 %	99.11 %	99.52 %	98.74 %
Liu et al. [59]	41.0 %	48.0 %	70.0 %	92.0 %
Saini et al. [60]	97.10 %	96.67 %	97.16 %	93.68 %
Our method	**99.8** %	**99.5** %	**98.9** %	**97.4** %

indicate that the proposed method is robust to the different levels of noise perturbations that decomposed with wavelet transform. This robustness test is an indication of the strong generalization ability of the designed strategy to perform accurate cancer classification by accepting a wide range of images with inevitable noise perturbations. Figure 7, shows the accuracy graph for ICIAR (Figure 7a) and BreakHis (Figure 7b) datasets contaminated with different levels of random noises.

B. ACCURACY COMPARISON WITH THE STATE-OF-THE-ART METHODS USING THE ICIAR 2018 HIDDEN TEST DATA

The test set of the ICIAR 2018 dataset consists of 100 images. The class labels of the ICIAR 2018 test dataset are not publicly available. Therefore, we evaluated the test results and submitted them online to the BACH challenge for evaluation. Our model achieved a higher recognition accuracy of 92%. The accuracy comparison with the legacy resultsLegacy-Results - Grand Challenge (grand-challenge.org) is given in Table 12. Table 12 shows that our model considerably outperforms the other state-of-the-art methods reported in [29].

The output results are also compared with the few most recent approaches where the CNN based approaches have been used on the BreakHis dataset. Spanhol et al. [54] performed the binary class classification of benign and malignant using the AlexNet model and achieved about 80.8% to 89.6% accuracy on the BreakHis dataset. In [55], Alom et al. reported the accuracies on the BreakHis dataset at different magnification factors. They obtained 97.09 $\pm$ 1.06 and 97.95 $\pm$ 1.07 accuracies at multi-class and binary-class classification at 40% magnification. In [56] Zhongyi Han et al. have designed a model called class-structured based deep convolutional neural network model (CSDCNN) and obtained accuracy from 93.5% to 97.1%. Al Nahid and Kong [57] proposed a strategy based on CNN and handcrafted features based and obtained accuracy between 94.40% and 97.19%. In [58], Gupta et al. designed a modified residual network and obtained accuracy between 98.16% and 99.66%. In [59], Liu et al. used an AlexNet-BC model to perform multi-class classification on the BreakHis dataset and achieved 94.67% accuracy. Recently, Saini and Susan [60] designed a VGGIN-Net by applying the transfer learning approach and obtained accuracy between 93.68% and 97.10%. In comparison to all the aforementioned reported results, our model shows promising performance. On the BreakHis dataset, our model obtained an accuracy of 99.8% on multiclass classification and 99.9% on binary class classification on different magnification images with minimum test time reported. The test time and accuracies are reported in Table 9 and Table 12, respectively. Table 13 shows the comparative analysis with state-of-the-art methods on BreakHis dataset.

TABLE 14. Comparative analysis of our proposed model with state-of-the-art method for 3-class classification using WSIs from bracs dataset [].

		Benign (%)	Atypical (%)	Malignant (%)	Total (%)
Brancati,N. et al [66]	F score	74.4	57.2	78.0	69.8
	Precision	75.6	51.5	86.5	71.2
	Sensitivity	72.5	65.2	71.9	69.9
	Accuracy	-	-	-	70.3
Proposed method	F score	79.1	63.3	84.2	75.5
	Precision	78.6	57.3	91.7	75.8
	Sensitivity	76.2	68.3	79.3	74.4
	Accuracy	75.3	66.2	74.5	72.2

C. PERFORMANCE ANALYSIS USING BRACS DATASET [65]

In order to check the validity of our proposed method on gigapixel whole slide images acquired with scanners,

new experiments have been conducted using WSI of recent Bracs dataset [65]. We performed the experiments using our proposed model for multi-class classification on the Bracs dataset. For the Bracs dataset, multi-class classification has been performed for the three classes of WSIs (Atypical, Benign, and Malignant classes). In experiments, we considered the 10× magnification WSIs to avoid the computational limits. Moreover, to avoid the network overfitting the normalized WSIs at 5× and 2.5× magnification was used. Our method integrates both global and local information, is flexible regarding the size of the input images and only requires weak image-level labels. On the Bracs dataset, comparative analysis has been performed with recent state-of-the-art convolution neural network proposed in [66]. On the Bracs dataset, we evaluated the results in terms of F-measure, precision, recall, and total accuracy, given in Table 14. The WSIs from Bracs dataset have variable resolution, the dimensions can easily exceed 100,000 by 100,000 pixels.

IV. CONCLUSION AND FUTURE WORK

Since deep CNN models are often over parameterized therefore their deployment for real time applications is challenging particularly for resource-constrained hardware. In this paper, a new automatic method, a lightweight deep CNN model for multi-class cancer categorization from breast histopathology images has been proposed. The proposed method solves the problem of increased computation caused by high-resolution input images network depth and width of the model. The Haar wavelet decomposition step and inverted residual block in the designed lightweight model vastly overcame major computational bottlenecks and enabled fast cancer classification from high size images. The method is validated on three benchmark histopathology datasets, and it yielded promising accuracy (96.2%, 99.8%, and 72.2%, for ICIAR 2018, BreakHis, and Bracs datasets, respectively) with less test time (i.e., 0.67s, 0.21s and 10.6s for ICIAR 2018, BreakHis, and Bracs images, respectively) for multi-class classification. The performance results show the robustness of the proposed method over the results of existing state-of-the-art techniques. However, this method shows few limitations; there is little tradeoff between the computational cost of our designed deep model and its output accuracy. The model trained on original size images shows good accuracy in comparison to models trained on decomposed images, as during the image decomposition step, some information is lost from input images. However, the automatic deep cancer detection models trained with original images express high computational costs which make them undesirable for real time applications. In the future, the impact of the depth of the model on its performance can be analyzed to effectively design an efficient and lightweight deep model. Future research work may also involve improving the efficiency of classifiers by developing the dataset with millions of breast histopathology images. Moreover, this method could be applied to other medical imaging modalities e.g., magnetic resonance imaging, computed tomography, and X-rays. The future goal also comprises designing a robust end-to-end cancer grading system to count tumor proliferation scores directly from whole-slide images.

CONFLICTS OF INTEREST

The authors have no conflicts of interest to declare.

REFERENCES

[1] R. L. Siegel, K. D. Miller, H. E. Fuchs, and A. Jemal, "Cancer statistics, 2022," *CA, Cancer J. Clinicians*, vol. 72, no. 1, pp. 7–33, Jan. 2022, doi: 10.3322/caac.21708.

[2] C. W. Elston and I. O. Ellis, "Pathological prognostic factors in breast cancer. I. The value of histological grade in breast cancer: Experience from a large study with long-term follow-up," *Histopathology*, vol. 19, no. 5, pp. 403–410, Nov. 1991, doi: 10.1111/j.1365-2559.1991.tb00229.x.

[3] D. Kaplun, A. Krasichkov, P. Chetyrbok, N. Oleinikov, A. Garg, and H. S. Pannu, "Cancer cell profiling using image moments and neural networks with model agnostic explainability: A case study of breast cancer histopathological (BreakHis) database," *Mathematics*, vol. 9, no. 20, p. 2616, Oct. 2021, doi: 10.3390/math9202616.

[4] F. Aeffner, K. Wilson, N. T. Martin, J. C. Black, C. L. L. Hendriks, B. Bolon, D. G. Rudmann, R. Gianani, S. R. Koegler, J. Krueger, and G. D. Young, "The gold standard paradox in digital image analysis: Manual versus automated scoring as ground truth," *Arch. Pathol. Lab. Med.*, vol. 141, no. 9, pp. 1267–1275, Sep. 2017, doi: 10.5858/arpa.2016-0386-RA.

[5] T. Kausar, M. Wang, M. A. Ashraf, and A. Kausar, "SmallMitosis: Small size mitotic cells detection in breast histopathology images," *IEEE Access*, vol. 9, pp. 905–922, 2021, doi: 10.1109/ACCESS.2020.3044625.

[6] A. Shabbir, A. Rasheed, H. Shehraz, A. Saleem, B. Zafar, M. Sajid, N. Ali, S. H. Dar, and T. Shehryar, "Detection of glaucoma using retinal fundus images: A comprehensive review," *Math. Biosci. Eng.*, vol. 18, no. 3, pp. 2033–2076, 2021, doi: 10.3934/MBE.2021106.

[7] S. K. Jafarbigloo and H. Danyali, "Nuclear atypia grading in breast cancer histopathological images based on CNN feature extraction and LSTM classification," *CAAI Trans. Intell. Technol.*, vol. 6, no. 4, pp. 426–439, Dec. 2021, doi: 10.1049/cit2.12061.

[8] Q. Zou, K. Xiong, Q. Fang, and B. Jiang, "Deep imitation reinforcement learning for self-driving by vision," *CAAI Trans. Intell. Technol.*, vol. 6, no. 4, pp. 493–503, Dec. 2021, doi: 10.1049/cit2.12025.

[9] A. Rasheed, B. Zafar, A. Rasheed, N. Ali, M. Sajid, S. H. Dar, U. Habib, T. Shehryar, and M. T. Mahmood, "Fabric defect detection using computer vision techniques: A comprehensive review," *Math. Problems Eng.*, vol. 2020, pp. 1–24, Nov. 2020, doi: 10.1155/2020/8189403.

[10] S. Fatima, N. A. Aslam, I. Tariq, and N. Ali, "Home security and automation based on Internet of Things: A comprehensive review," *IOP Conf. Ser., Mater. Sci. Eng.*, vol. 899, no. 1, Jul. 2020, Art. no. 012011, doi: 10.1088/1757-899X/899/1/012011.

[11] K. George, S. Faziludeen, P. Sankaran, and K. P. Joseph, "Breast cancer detection from biopsy images using nucleus guided transfer learning and belief based fusion," *Comput. Biol. Med.*, vol. 124, Sep. 2020, Art. no. 103954, doi: 10.1016/j.compbiomed.2020.103954.

[12] C. Kaushal, S. Bhat, D. Koundal, and A. Singla, "Recent trends in computer assisted diagnosis (CAD) system for breast cancer diagnosis using histopathological images," *IRBM*, vol. 40, no. 4, pp. 211–227, Aug. 2019, doi: 10.1016/j.irbm.2019.06.001.

[13] T. Kausar, A. Kausar, M. A. Ashraf, M. F. Siddique, M. Wang, M. Sajid, M. Z. Siddique, A. U. Haq, and I. Riaz, "SA-GAN: Stain acclimation generative adversarial network for histopathology image analysis," *Appl. Sci.*, vol. 12, no. 1, p. 288, Dec. 2021, doi: 10.3390/app12010288.

[14] K. Medhi, M. Jamil, and M. I. Hussain, "Automatic detection of COVID-19 infection from chest X-ray using deep learning," *medRxiv*, 2020, doi: 10.1101/2020.05.10.20097063.

[15] M. A. Khan, M. Sharif, T. Akram, S. Kadry, and C. Hsu, "A two-stream deep neural network-based intelligent system for complex skin cancer types classification," *Int. J. Intell. Syst.*, vol. 37, no. 12, pp. 10621–10649, Dec. 2022, doi: 10.1002/int.22691.

[16] B. A. Skourt, A. E. Hassani, and A. Majda, "Lung CT image segmentation using deep neural networks," *Proc. Comput. Sci.*, vol. 127, pp. 109–113, Jan. 2018, doi: 10.1016/J.PROCS.2018.01.104.

[17] M. Salvi, U. R. Acharya, F. Molinari, and K. M. Meiburger, "The impact of pre- and post-image processing techniques on deep learning frameworks: A comprehensive review for digital pathology image analysis," *Comput. Biol. Med.*, vol. 128, Jan. 2021, Art. no. 104129, doi: 10.1016/J.COMPBIOMED.2020.104129.

[18] A. B. Hamida, M. Devanne, J. Weber, C. Truntzer, V. Derangère, F. Ghiringhelli, G. Forestier, and C. Wemmert, "Deep learning for colon cancer histopathological images analysis," *Comput. Biol. Med.*, vol. 136, Sep. 2021, Art. no. 104730, doi: 10.1016/J.COMPBIOMED.2021.104730.

[19] S. Wang, D. M. Yang, R. Rong, X. Zhan, and G. Xiao, "Pathology image analysis using segmentation deep learning algorithms," *Amer. J. Pathol.*, vol. 189, no. 9, pp. 1686–1698, Sep. 2019, doi: 10.1016/J.AJPATH.2019.05.007.

[20] G. Chugh, S. Kumar, and N. Singh, "Survey on machine learning and deep learning applications in breast cancer diagnosis," *Cogn. Comput.*, vol. 13, no. 6, pp. 1451–1470, Nov. 2021, doi: 10.1007/s12559-020-09813-6.

[21] J. Bai, R. Posner, T. Wang, C. Yang, and S. Nabavi, "Applying deep learning in digital breast tomosynthesis for automatic breast cancer detection: A review," *Med. Image Anal.*, vol. 71, Jul. 2021, Art. no. 102049, doi: 10.1016/J.MEDIA.2021.102049.

[22] K. Rautela, D. Kumar, and V. Kumar, "A systematic review on breast cancer detection using deep learning techniques," *Arch. Comput. Methods Eng.*, vol. 29, no. 7, pp. 4599–4629, Nov. 2022, doi: 10.1007/s11831-022-09744-5.

[23] K. Roy, D. Banik, D. Bhattacharjee, and M. Nasipuri, "Patch-based system for classification of breast histology images using deep learning," *Comput. Med. Imag. Graph.*, vol. 71, pp. 90–103, Jan. 2019, doi: 10.1016/j.compmedimag.2018.11.003.

[24] E. T. Zewdie, A. W. Tessema, and G. L. Simegn, "Classification of breast cancer types, sub-types and grade from histopathological images using deep learning technique," *Health Technol.*, vol. 11, no. 6, pp. 1277–1290, Nov. 2021, doi: 10.1007/s12553-021-00592-0.

[25] T. Araújo, G. Aresta, E. Castro, J. Rouco, P. Aguiar, C. Eloy, A. Polónia, and A. Campilho, "Classification of breast cancer histology images using convolutional neural networks," *PLoS One*, vol. 12, no. 6, 2017, Art. no. e0177544, doi: 10.1371/journal.pone.0177544.

[26] S. Khan, N. Islam, Z. Jan, I. U. Din, and J. J. P. C. Rodrigues, "A novel deep learning based framework for the detection and classification of breast cancer using transfer learning," *Pattern Recognit. Lett.*, vol. 125, pp. 1–6, Jul. 2019, doi: 10.1016/j.patrec.2019.03.022.

[27] Z. Hameed, S. Zahia, B. Garcia-Zapirain, J. J. Aguirre, and A. M. Vanegas, "Breast cancer histopathology image classification using an ensemble of deep learning models," *Sensors*, vol. 20, no. 16, p. 4373, Aug. 2020, doi: 10.3390/s20164373.

[28] R. Yan, F. Ren, Z. Wang, L. Wang, T. Zhang, Y. Liu, X. Rao, C. Zheng, and F. Zhang, "Breast cancer histopathological image classification using a hybrid deep neural network," *Methods*, vol. 173, pp. 52–60, Feb. 2020, doi: 10.1016/j.ymeth.2019.06.014.

[29] G. Aresta et al., "BACH: Grand challenge on breast cancer histology images," *Med. Image Anal.*, vol. 56, pp. 122–139, Aug. 2019, doi: 10.1016/j.media.2019.05.010.

[30] Y. S. Vang, Z. Chen, and X. Xie, "Deep learning framework for multi-class breast cancer histology image classification," in *Proc. Int. Conf. Image Anal. Recognit.*, 2018, pp. 914–922, doi: 10.1007/978-3-319-93000-8_104.

[31] C. Szegedy, V. Vanhoucke, S. Ioffe, J. Shlens, and Z. Wojna, "Rethinking the inception architecture for computer vision," in *Proc. IEEE Conf. Comput. Vis. Pattern Recognit. (CVPR)*, Jun. 2016, pp. 2818–2826, doi: 10.1109/CVPR.2016.308.

[32] A. Rakhlin, A. Shvets, V. Iglovikov, and A. A. Kalinin, "Deep convolutional neural networks for breast cancer histology image analysis," in *Proc. Int. Conf. Image Anal. Recognit.*, 2018, pp. 737–744, doi: 10.1007/978-3-319-93000-8_83.

[33] R. Awan, N. A. Koohbanani, M. Shaban, A. Lisowska, and N. Rajpoot, "Context-aware learning using transferable features for classification of breast cancer histology images," in *Proc. Int. Conf. Image Anal. Recognit.*, 2018, pp. 788–795, doi: 10.1007/978-3-319-93000-8_89.

[34] K. He and J. Sun, "Convolutional neural networks at constrained time cost," in *Proc. IEEE Conf. Comput. Vis. Pattern Recognit.*, Jun. 2015, pp. 5353–5360, doi: 10.1109/CVPR.2015.7299173.

[35] I. Daubechies, "Ten lectures on wavelets," *Math. Comput.*, vol. 61, no. 204, p. 941, Oct. 1993, doi: 10.2307/2153268.

[36] S. G. Mallat, "A theory for multiresolution signal decomposition: The wavelet representation," *IEEE Trans. Pattern Anal. Mach. Intell.*, vol. 11, no. 7, pp. 674–693, Jul. 1989, doi: 10.1109/34.192463.

[37] P. Liu, H. Zhang, K. Zhang, L. Lin, and W. Zuo, "Multi-level wavelet-CNN for image restoration," in *Proc. IEEE/CVF Conf. Comput. Vis. Pattern Recognit. Workshops (CVPRW)*, Jun. 2018, pp. 773–782, doi: 10.1109/CVPRW.2018.00121.

[38] T. Williams and R. Li, "Wavelet pooling for convolutional neural networks," Tech. Rep., 2018.

[39] J. Yoo, Y. Uh, S. Chun, B. Kang, and J.-W. Ha, "Photorealistic style transfer via wavelet transforms," in *Proc. IEEE/CVF Int. Conf. Comput. Vis. (ICCV)*, Oct. 2019, pp. 9036–9045, doi: 10.1109/ICCV.2019.00913.

[40] T. Chen, "Learning a wavelet-like auto-encoder to accelerate deep neural networks," 2017, *arXiv:1712.07493*.

[41] S. Fujieda, K. Takayama, and T. Hachisuka, "Wavelet convolutional neural networks for texture classification," 2017, *arXiv:1707.07394*.

[42] T. Wan, X. Liu, J. Chen, and Z. Qin, "Wavelet-based statistical features for distinguishing mitotic and non-mitotic cells in breast cancer histopathology," in *Proc. IEEE Int. Conf. Image Process. (ICIP)*, Oct. 2014, pp. 2290–2294, doi: 10.1109/ICIP.2014.7025464.

[43] S. I. Niwas, P. Palanisamy, K. Sujathan, and E. Bengtsson, "Analysis of nuclei textures of fine needle aspirated cytology images for breast cancer diagnosis using complex Daubechies wavelets," *Signal Process.*, vol. 93, no. 10, pp. 2828–2837, 2013, doi: 10.1016/j.sigpro.2012.06.029.

[44] R. Karthiga and K. Narasimhan, "Automated diagnosis of breast cancer using wavelet based entropy features," in *Proc. 2nd Int. Conf. Electron., Commun. Aerosp. Technol. (ICECA)*, Mar. 2018, pp. 274–279, doi: 10.1109/ICECA.2018.8474739.

[45] R. C. Gonzalez, R. E. Woods, and B. R. Masters, "Digital image processing, third edition," *Proc. SPIE*, vol. 14, no. 2, 2009, Art. no. 029901, doi: 10.1117/1.3115362.

[46] K. Simonyan and A. Zisserman, "Very deep convolutional networks for large-scale image recognition," 2015, *arXiv:1409.1556*.

[47] K. He, X. Zhang, S. Ren, and J. Sun, "Deep residual learning for image recognition," in *Proc. IEEE Conf. Comput. Vis. Pattern Recognit. (CVPR)*, Jun. 2016, pp. 770–778, doi: 10.1109/CVPR.2016.90.

[48] G. Huang, Z. Liu, L. Van Der Maaten, and K. Q. Weinberger, "Densely connected convolutional networks," in *Proc. IEEE Conf. Comput. Vis. Pattern Recognit. (CVPR)*, Jul. 2017, pp. 4700–4708, doi: 10.1109/CVPR.2017.243.

[49] A. Krizhevsky, I. Sutskever, and G. E. Hinton, "ImageNet classification with deep convolutional neural networks," *Commun. ACM*, vol. 60, no. 6, pp. 84–90, May 2017, doi: 10.1145/3065386.

[50] M. Sandler, A. Howard, M. Zhu, A. Zhmoginov, and L.-C. Chen, "MobileNetV2: Inverted residuals and linear bottlenecks," in *Proc. IEEE/CVF Conf. Comput. Vis. Pattern Recognit.*, Jun. 2018, pp. 4510–4520, doi: 10.1109/CVPR.2018.00474.

[51] P. Y. Simard, D. Steinkraus, and J. C. Platt, "Best practices for convolutional neural networks applied to visual document analysis," in *Proc. ICDAR*, 2003, pp. 1–6, doi: 10.1109/ICDAR.2003.1227801.

[52] R. Olivier and C. Hanqiang, "Nearest neighbor value interpolation," *Int. J. Adv. Comput. Sci. Appl.*, vol. 3, no. 4, pp. 1–6, 2012, doi: 10.14569/ijacsa.2012.030405.

[53] A. Gupta, Anjum, S. Gupta, and R. Katarya, "InstaCovNet-19: A deep learning classification model for the detection of COVID-19 patients using chest X-ray," *Appl. Soft Comput.*, vol. 99, Feb. 2021, Art. no. 106859, doi: 10.1016/j.asoc.2020.106859.

[54] F. A. Spanhol, L. S. Oliveira, C. Petitjean, and L. Heutte, "Breast cancer histopathological image classification using convolutional neural networks," in *Proc. Int. Joint Conf. Neural Netw. (IJCNN)*, Jul. 2016, pp. 2560–2567, doi: 10.1109/IJCNN.2016.7727519.

[55] M. Z. Alom, C. Yakopcic, M. S. Nasrin, T. M. Taha, and V. K. Asari, "Breast cancer classification from histopathological images with inception recurrent residual convolutional neural network," *J. Digit. Imag.*, vol. 32, no. 4, pp. 605–617, Aug. 2019, doi: 10.1007/s10278-019-00182-7.

[56] Z. Han, B. Wei, Y. Zheng, Y. Yin, K. Li, and S. Li, "Breast cancer multi-classification from histopathological images with structured deep learning model," *Sci. Rep.*, vol. 7, no. 1, Jun. 2017, Art. no. 4172, doi: 10.1038/s41598-017-04075-z.

[57] A.-A. Nahid and Y. Kong, "Histopathological breast-image classification using local and frequency domains by convolutional neural network," *Information*, vol. 9, no. 1, p. 19, Jan. 2018, doi: 10.3390/info9010019.

[58] V. Gupta, M. Vasudev, A. Doegar, and N. Sambyal, "Breast cancer detection from histopathology images using modified residual neural networks," *Biocybern. Biomed. Eng.*, vol. 41, no. 4, pp. 1272–1287, Oct. 2021, doi: 10.1016/j.bbe.2021.08.011.
[59] M. Liu, L. Hu, Y. Tang, C. Wang, Y. He, C. Zeng, K. Lin, Z. He, and W. Huo, "A deep learning method for breast cancer classification in the pathology images," *IEEE J. Biomed. Health Informat.*, vol. 26, no. 10, pp. 5025–5032, Oct. 2022, doi: 10.1109/JBHI.2022.3187765.
[60] M. Saini and S. Susan, "Deep transfer with minority data augmentation for imbalanced breast cancer dataset," *Appl. Soft Comput.*, vol. 97, Dec. 2020, Art. no. 106759, doi: 10.1016/j.asoc.2020.106759.
[61] T. Araújo et al. *Grand Challenge on Breast Cancer Histology Images(BACH) ICIAR*. [Online]. Available: https://iciar2018-challenge.grand-challenge.org/
[62] T. Kausar, M. Wang, M. Idrees, and Y. Lu, "HWDCNN: Multi-class recognition in breast histopathology with Haar wavelet decomposed image based convolution neural network," *Biocybern. Biomed. Eng.*, vol. 39, no. 4, pp. 967–982, Oct. 2019.
[63] M. Zamir, N. Ali, A. Naseem, A. A. Frasteen, B. Zafar, M. Assam, M. Othman, and E.-A. Attia, "Face detection & recognition from images & videos based on CNN & Raspberry Pi," *Computation*, vol. 10, no. 9, p. 148, Aug. 2022.
[64] L. Mampitiya, N. Rathnayake, and S. De Silva, "Efficient and low-cost skin cancer detection system implementation with a comparative study between traditional and CNN-based models," *J. Comput. Cogn. Eng.*, vol. 2, no. 3, pp. 226–235, 2022.
[65] [Online]. Available: https://www.bracs.icar.cnr.it/
[66] N. Brancati, G. De Pietro, D. Riccio, and M. Frucci, "Gigapixel histopathological image analysis using attention-based neural networks," *IEEE Access*, vol. 9, pp. 87552–87562, 2021, doi: 10.1109/ACCESS.2021.3086892.
[67] F. Masood, J. Masood, H. Zahir, K. Driss, N. Mehmood, and H. Farooq, "Novel approach to evaluate classification algorithms and feature selection filter algorithms using medical data," *J. Comput. Cogn. Eng.*, vol. 2, no. 1, pp. 57–67, May 2022.
[68] S. B. Mallikarjuna, P. Shivakumara, V. Khare, M. Basavanna, U. Pal, and B. Poornima, "Multi-gradient-direction based deep learning model for arecanut disease identification," *CAAI Trans. Intell. Technol.*, vol. 7, no. 2, pp. 156–166, Jun. 2022.
[69] M. Zheng, K. Zhi, J. Zeng, C. Tian, and L. You, "A hybrid CNN for image denoising," *J. Artif. Intell. Technol.*, vol. 2, no. 3, pp. 93–99, Apr. 2022.
[70] Q. Zhang, J. Xiao, C. Tian, J. C.-W. Lin, and S. Zhang, "A robust deformed convolutional neural network (CNN) for image denoising," *CAAI Trans. Intell. Technol.*, vol. 8, no. 2, pp. 331–342, Jun. 2023.
[71] J. Meng, Y. Li, H. Liang, and Y. Ma, "Single image dehazing based on two-stream convolutional neural network," *J. Artif. Intell. Technol.*, vol. 2, no. 3, pp. 100–110, Jun. 2022.
[72] F. Ahmad, "Deep image retrieval using artificial neural network interpolation and indexing based on similarity measurement," *CAAI Trans. Intell. Technol.*, vol. 7, no. 2, pp. 200–218, Jun. 2022.

TASLEEM KAUSAR was born in Pakistan, in 1988. She received the B.Sc. degree in electrical engineering from The University of Azad Jammu and Kashmir, Pakistan, in 2010, the M.Sc. degree in electronics engineering from the University of Engineering and Technology, Taxila, Pakistan, in 2013, and the Ph.D. degree in electronics from the Harbin Institute of China, in 2020. She is currently an Assistant Professor with the Mirpur University of Science and Technology, Pakistan. Her research interest includes medical image analysis using deep learning techniques.

YUN LU was born in Hengyang, Hunan, China, in 1985. He received the B.S. degree in microelectronics from Xiangtan University, Hunan, in 2009, the M.S. degree in optical engineering from Sun Yat-sen University, China, in 2011, and the Ph.D. degree in microelectronics and solid state electronics from the Harbin Institute of Technology, Shenzhen, China, in 2020. From 2011 to 2014, he was with the Shenzhen Institute of Advanced Technology, Chinese Academy of Sciences, working on the design of mixed signal front-end circuits for biomedical applications. From 2014 to 2017, he was a Senior Engineer with Launch Tech Company Ltd. Since August 2020, he has been an Associate Professor with Huizhou University, Guangdong, China. His current research interests include cognitive computing from neuroscience to engineering, innovative methods for brain–machine interface, and machine learning.

ADEEBA KAUSAR received the B.Sc. degree in computer system engineering from The University of Azad Jammu and Kashmir, Pakistan, in 2017, and the M.Sc. degree in computer system engineering from the University of Engineering and Technology, Taxila, Pakistan, in 2020.

She is currently a Lecturer with the Department of Information Engineering Technology, Superior University, Lahore, Pakistan. Her research interests include computer vision, image processing, and deep learning techniques.